

Demonstration of GaN-Based HEMTs Using Extremely Thin h-BN Passivation Layer and Air Spacer for the RF Performance Improvement

Sung-Jae Chang,* Seokho Moon, Junhyung Jeong, Hyun-Wook Jung, Jawon Kim, Semi Im, Jaesub Song, Changuk Ji, Seonghyeon Pak, Il-Gyu Choi, Youn-Sub Noh, Seong-Il Kim, Sang-Heung Lee, Ho-Kyun Ahn, Dong-Min Kang, Jong Kyu Kim, and Jong-Won Lim

GaN-based high electron mobility transistors (HEMTs) is demonstrated using an extremely thin (≈ 5 nm) h-BN passivation layer and air spacer, for the first time. The h-BN passivation layer is grown by metal–organic chemical vapor deposition on top of the AlGaN barrier, followed by GaN-based HEMTs fabrication. To prohibit the loss and/or damage of the thin h-BN passivation layer, the SiN is deposited as a protection layer during the device fabrication. When the device fabrication is finalized, the SiN protection layer is removed by buffered oxide etchant, introducing the air spacer under the head of the T-gate electrode. The electrical properties of the GaN-based HEMTs applying h-BN passivation layer and air spacer are measured and compared to the h-BN/SiN passivated and conventional SiN passivated GaN-based HEMTs. The difference of the DC characteristics corresponding to the passivation layer in GaN-based HEMTs is negligible. However, compared to the conventional SiN passivated GaN-based HEMTs, the RF performance, such as current gain cut-off frequency and maximum oscillation frequency is improved by 50.3% and 68.5%, respectively, since the parasitic capacitances is reduced by the air spacer formation in GaN-based HEMTs using a thin h-BN passivation layer.

1. Introduction

GaN-based high electron mobility transistors (HEMTs) have been intensively studied and developed for the high-power microwave application due to the superior material properties such as wide band-gap, high breakdown field, and high carrier density and mobility at the hetero-interface.^[1–3] However, there are many dangling bonds at the barrier layer surface which cause the leakage current increasement, drain current (I_D) reduction, current collapse enhancement, and frequency performance degradation.^[4–8] Therefore, in GaN-based HEMTs, the passivation layer deposited on top of the barrier layer, which was required excellent interface quality is essential. In this perspective, various dielectric layers and structures have been investigated as the passivation layer in GaN-based HEMTs.^[4,5,9–16]

In GaN-based HEMTs, the current gain cut-off frequency (f_T) and maximum oscillation frequency (f_{max}) are the key

indicators which reflect the RF performance. The f_T and f_{max} are determined by the several components of the small-signal equivalent circuit as follows:^[17,18]

$$f_T = \frac{g_m}{2\pi (C_{gs} + C_{gd}) [1 + (R_s + R_d) g_{ds}] + C_{gd} g_m (R_s + R_d)} \quad (1)$$

$$f_{max} = \frac{f_T}{2\sqrt{((R_g + R_s + R_{gs}) g_{ds} + 2\pi f_T C_{gd} R_g)}} \quad (2)$$

where g_m is the transconductance, and the other parameters are described in the small-signal equivalent circuits as shown in **Figure 1**. The RF performance is affected by the parasitic capacitances, including the gate-source capacitance (C_{gs}) and gate-drain capacitance (C_{gd}) even though, the impact of the other parameters cannot be neglected. As a result, the parasitic capacitances should be minimized for the RF performance improvement.^[19]

S.-J. Chang, J. Jeong, H.-W. Jung, I.-G. Choi, Y.-S. Noh, S.-I. Kim, S.-H. Lee, H.-K. Ahn, D.-M. Kang, J.-W. Lim
RF & Power component research section
Photonic & Wireless Device Research Division
Electronics and Telecommunications Research Institute
Daejeon 34129, Republic of Korea
E-mail: sjchang@etri.re.kr

S. Moon, J. Kim, S. Im, J. Song, C. Ji, S. Pak, J. K. Kim
Department of Materials Science and Engineering
Pohang University of Science and Technology
Pohang 37673, Republic of Korea

The ORCID identification number(s) for the author(s) of this article can be found under <https://doi.org/10.1002/aelm.202500638>

© 2025 The Author(s). Advanced Electronic Materials published by Wiley-VCH GmbH. This is an open access article under the terms of the [Creative Commons Attribution](https://creativecommons.org/licenses/by/4.0/) License, which permits use, distribution and reproduction in any medium, provided the original work is properly cited.

DOI: 10.1002/aelm.202500638

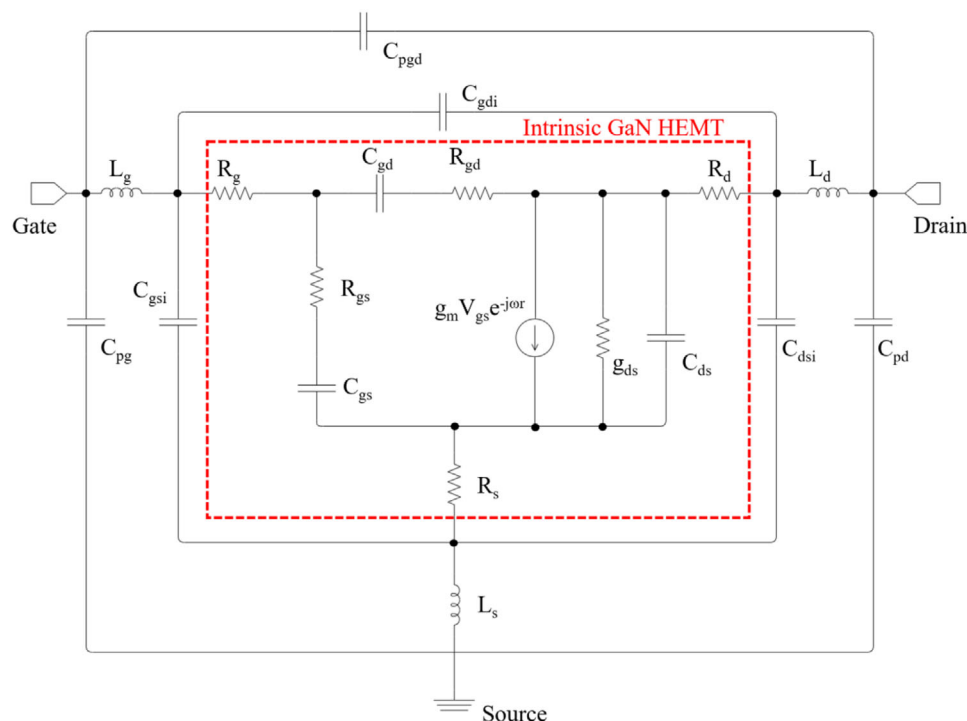


Figure 1. Small-signal equivalent circuit model of GaN-based HEMTs.

When the GaN-based HEMTs were compared to the other competitive technologies, such as GaAs- and InP-based HEMTs, the GaN-based HEMTs exhibit higher output power. However, the RF performance in terms of the f_T and f_{max} is lower than that of the other technologies. In order to overcome this issue, many approaches have been researched, such as the T-gate electrode structure optimization, surface passivation, thin barrier epitaxial structure, n^+ -regrown source-drain contact, and graded channel.^[20–32]

Among the various approaches, the T-gate electrode has been commonly applied to improve the RF performance through the reduction of gate resistance (R_g). With increasing the wideness of the T-gate head, the R_g is reduced. However, the parasitic gate capacitances increased as the area under the head of the T-gate electrode widened. Therefore, for the improvement of the RF performance in GaN-based HEMTs, the parasitic capacitances should be reduced while the increase of the R_g is minimized.

In this paper, we demonstrated the T-gate electrode incorporating the extremely thin (≈ 5 nm) h-BN passivation layer and air spacer to enhance the RF performance in GaN-based HEMTs. The thin h-BN passivation layer was grown by metal organic chemical vapor deposition (MOCVD) on top of the AlGaN barrier. The MOCVD-grown h-BN layer provided a Van der Waals heterostructure with an AlGaN/GaN epitaxial layer.^[33,34] To protect the loss and/or damage of the h-BN passivation layer from the device fabrication, the 75 nm-thick SiN protection layer was deposited by a plasma-enhanced chemical vapor deposition (PECVD). After the T-gate electrode formation, the SiN protection layer was removed by the buffered oxide etch (BOE). The h-BN passivation layer was not removed since, the h-BN showed strong resistance to BOE. Thereby, the thin h-BN only passivation

layer and air spacer located under the head of the T-gate electrode were simultaneously achieved. The dielectric constant of the air was smaller than the dielectric constant of SiN. As a result, the parasitic capacitances were reduced and the f_T and f_{max} were improved by 50.3% and 68.5%, respectively, which compared to the conventional SiN passivated GaN-based HEMTs.

2. Device Fabrication

We have fabricated the GaN-based HEMTs applied extremely thin passivation layer and an air spacer. The AlGaN/GaN heterostructure was grown by MOCVD on a 2-inch SiC substrate. The grown epitaxial structure was composed of a 2 μm -thick Fe-doped GaN buffer, 100 nm-thick GaN channel, and 25 nm-thick $\text{Al}_{0.25}\text{Ga}_{0.75}\text{N}$ barrier. The thin h-BN passivation layer was grown on the AlGaN barrier using MOCVD in Prof. J. Kim's laboratory at POSTECH. The detailed h-BN growth was described elsewhere.^[33,34] A 50 nm-thick SiN protection layer was deposited by the PECVD on the h-BN passivation layer. For the source and drain ohmic metal deposition, the source and drain electrode areas were patterned using the i-line stepper. The 50 nm-thick SiN and thin h-BN layers were etched by a reactive ion etching (RIE) system, and Ti/Al/Ni/Au was deposited using an e-beam evaporator. In order to avoid the diffusion of the alloying metal into the SiN protection layer for the followed RTA process, the 50 nm-thick SiN protection layer was removed by BOE. For the source and drain ohmic contact formation, the RTA was performed at 880 $^\circ\text{C}$ for 30 s. The 50 nm-thick SiN protection layer was deposited, again. The phosphorus was implanted outside of the device active area for the device isolation. The 50 nm-thick SiN layer was removed since, the SiN protection layer was damaged

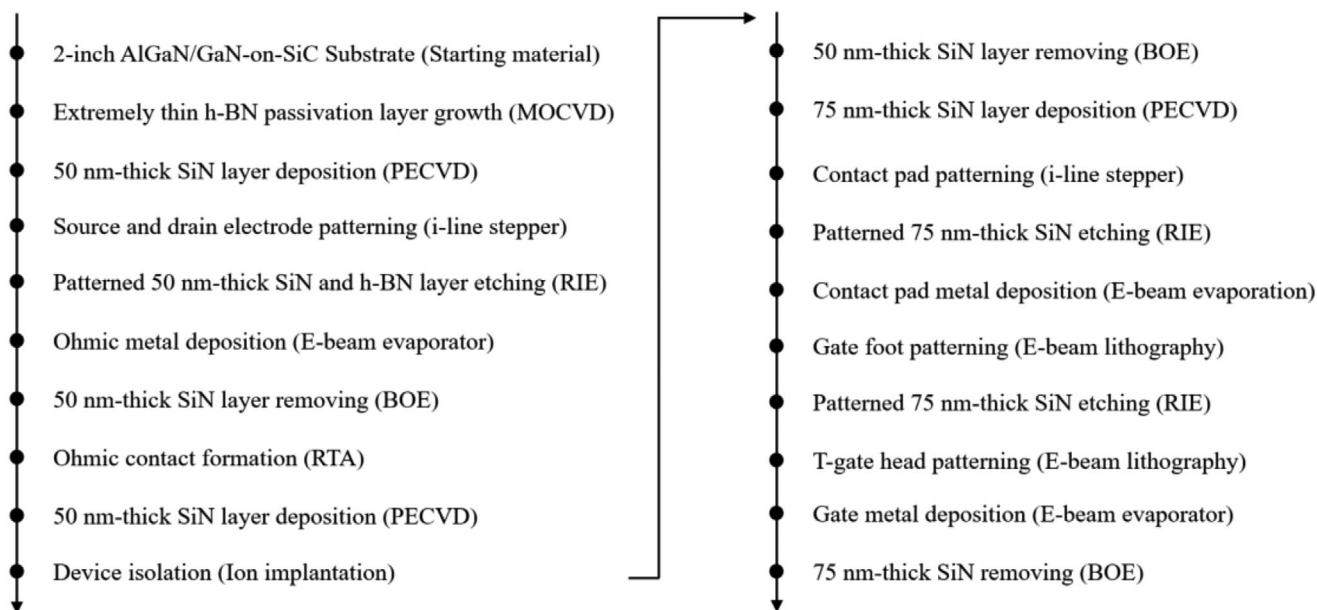


Figure 2. Summarized GaN-based HEMTs process flow applied in this work.

during the phosphorous implantation. The 75 nm-thick SiN protection layer was deposited one more time. The source and drain contact pads were defined and opened using the i-line stepper and RIE, respectively. Ti/Au was deposited for the contact pad formation. The gate foot (i.e., gate length) was patterned by the e-beam lithography. The 75 nm-thick SiN and thin h-BN layers were etched to open the gate foot region using an inductively coupled plasma. Then, the e-beam lithography was used for the T-gate head patterning. To form the T-gate electrode, Ni/Au was deposited by the e-beam evaporator. Finally, the processed wafer was dipped into the BOE to remove the 75 nm-thick SiN protection layer, remaining only the thin h-BN passivation layer and forming the air spacer under the T-gate head. In Figure 2, the GaN-based HEMTs process flow which was applied in this work was summarized.

Three BOE etching processes were carried out during the GaN-based HEMTs fabrication. To verify that the BOE etching process did not impact device performance, measurements were performed using TLM and process control monitoring patterns following the completion of each process step. However, we could not observe any evidences of device performance degradation attributable to BOE etching.

The gate length (L_G), unit gate width (W_G), and number of fingers (N_F) of the processed devices were 0.15, 100, and 2 μm , respectively. While the distance between source and gate (L_{SG}) was fixed as 1 μm , the distance between gate and drain (L_{GD}) were prepared for 1.85 and 2.85 μm . Therefore, the two different dimensional devices were processed. The distance between source and drain (L_{SD}) were 3 and 4 μm corresponding to the L_{GD} . The h-BN/SiN and conventional SiN passivated GaN-based HEMTs were simultaneously prepared for the comparison of the device characteristics. The h-BN, h-BN/SiN, and SiN passivated GaN-based HEMTs were designated as the Sample A, Sample B, and Sample C, respectively. Figure 3 showed the cross-sectional view of the GaN-based HEMTs for the three different samples.

3. Results and Discussion

In Figure 4, we have presented a detailed microstructural analysis of the MOCVD-grown h-BN passivation layer on the AlGaIn/GaN heterostructure. Figure 4a showed a high-resolution transmission electron microscopy (HR-TEM) image of the as-grown h-BN on the AlGaIn/GaN HEMT epi-structure, revealing a uniform h-BN layer with a thickness of ≈ 5 nm. The corresponding fast

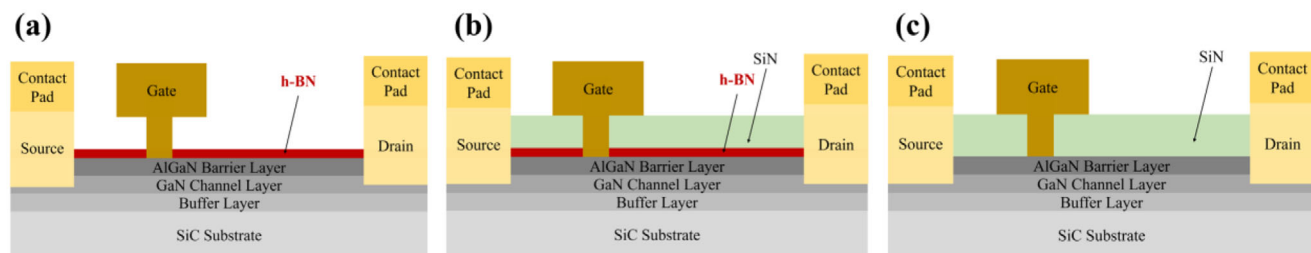


Figure 3. Schematic cross-sectional view of the fabricated GaN-based HEMTs in this paper. a) thin h-BN (Sample A), b) h-BN/SiN (Sample B), and c) SiN (Sample C) passivated GaN-based HEMTs.

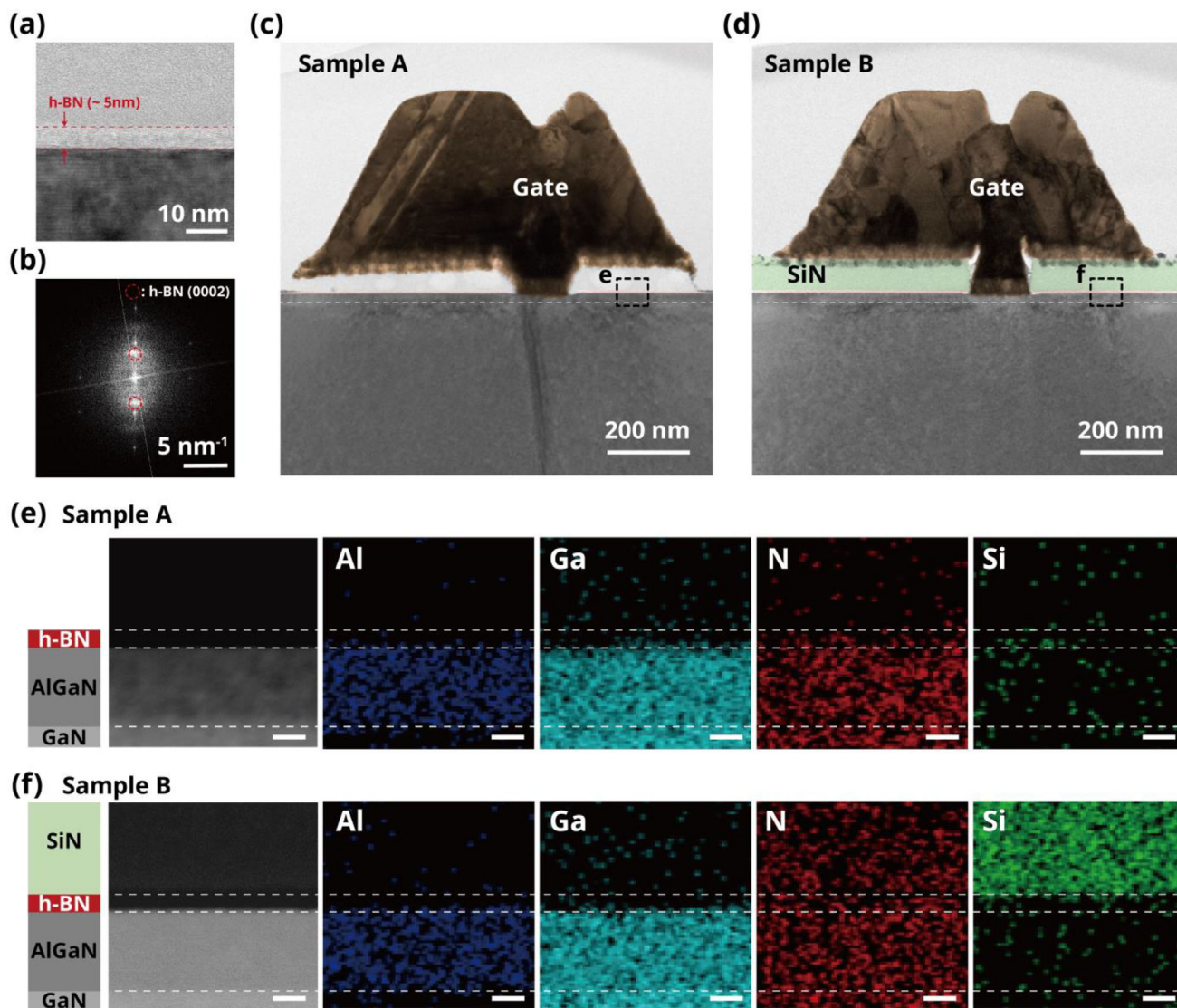


Figure 4. a) Cross-sectional TEM image of MOCVD-grown h-BN on AlGaN/GaN HEMT epi-structure and b) the corresponding fast Fourier transform image. False-colored Low-magnification TEM micrographs obtained from c) Sample A and d) Sample B, respectively, where yellow, green, and red represented gate, SiN and h-BN, respectively. Cross-sectional HAADF-STEM images with schematic structure diagrams and EDS elemental mapping analysis for e) Sample A and f) Sample B at locations indicated in (c) and (d), respectively. Scale bars, 10 nm.

Fourier transform (FFT) pattern in Figure 4b exhibited distinct (0002) diffraction spots characteristic of h-BN, which confirmed the epitaxial growth of crystalline h-BN on the AlGaN/GaN heterostructure.

Low-magnification cross-sectional TEM micrographs of Sample A and Sample B were presented in Figure 4c,d, respectively, showing the distinct configurations of the passivation layers. To further investigate the elemental distribution and interface quality, high-angle annular dark-field scanning transmission electron microscopy (HAADF-STEM) coupled with energy dispersive X-ray spectroscopy (EDS) mapping was performed at specific regions indicated in Figure 3c,d. The HAADF-STEM images combined with EDS elemental mapping analyses (Figure 3e,f) clearly demonstrated that the AlGaN/GaN heterostructure remained intact after the h-BN growth process, which reflected that the high-

temperature MOCVD-grown h-BN did not deteriorate the underlying device structure.

Notably, the EDS analysis revealed a significant difference between Sample A and Sample B. In Sample A, the area above the h-BN layer appeared vacant, consistent with the successful removal of the SiN protection layer and formation of the air spacer. In contrast, Sample B exhibited the uniform SiN passivation layer ≈ 75 nm thick deposited on top of the h-BN film, as evidenced by the strong Si signal in the EDS mapping. This microstructural evidence confirmed the successful implementation of our fabrication strategy, particularly the selective removal of the SiN protection layer in Sample A while preserving the thin h-BN passivation layer, which was critical for the formation of the air spacer under the head of the T-gate electrode.

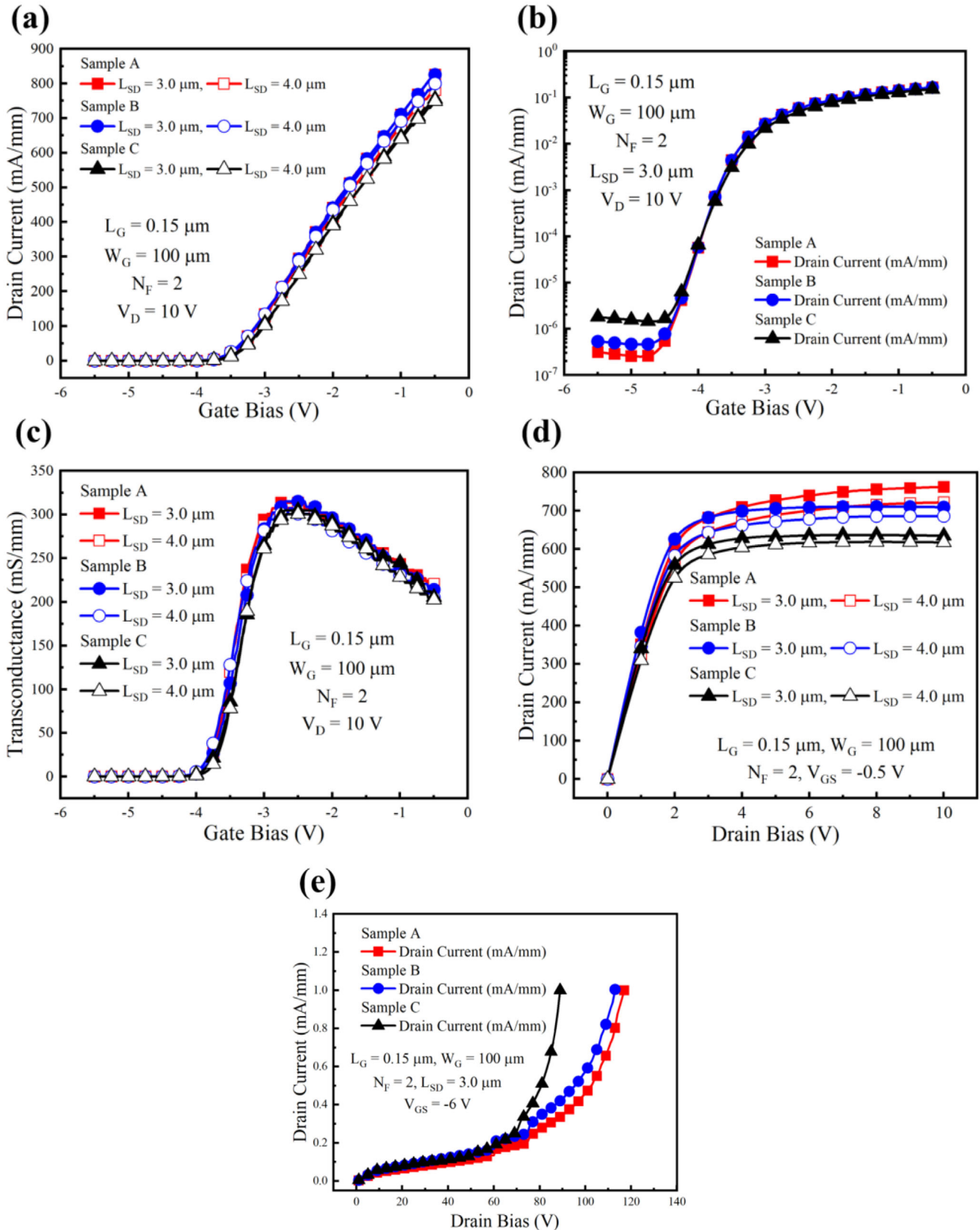


Figure 5. DC characteristics of GaN-based HEMTs for various passivation layers. a) Drain current in linear scale, b) drain current in log scale, and c) transconductance as a function of V_{GS} at $V_D = 10.0 \text{ V}$, Drain current vs drain bias at (d) $V_{GS} = -1.0 \text{ V}$ and (e) $V_{GS} = -6.0 \text{ V}$.

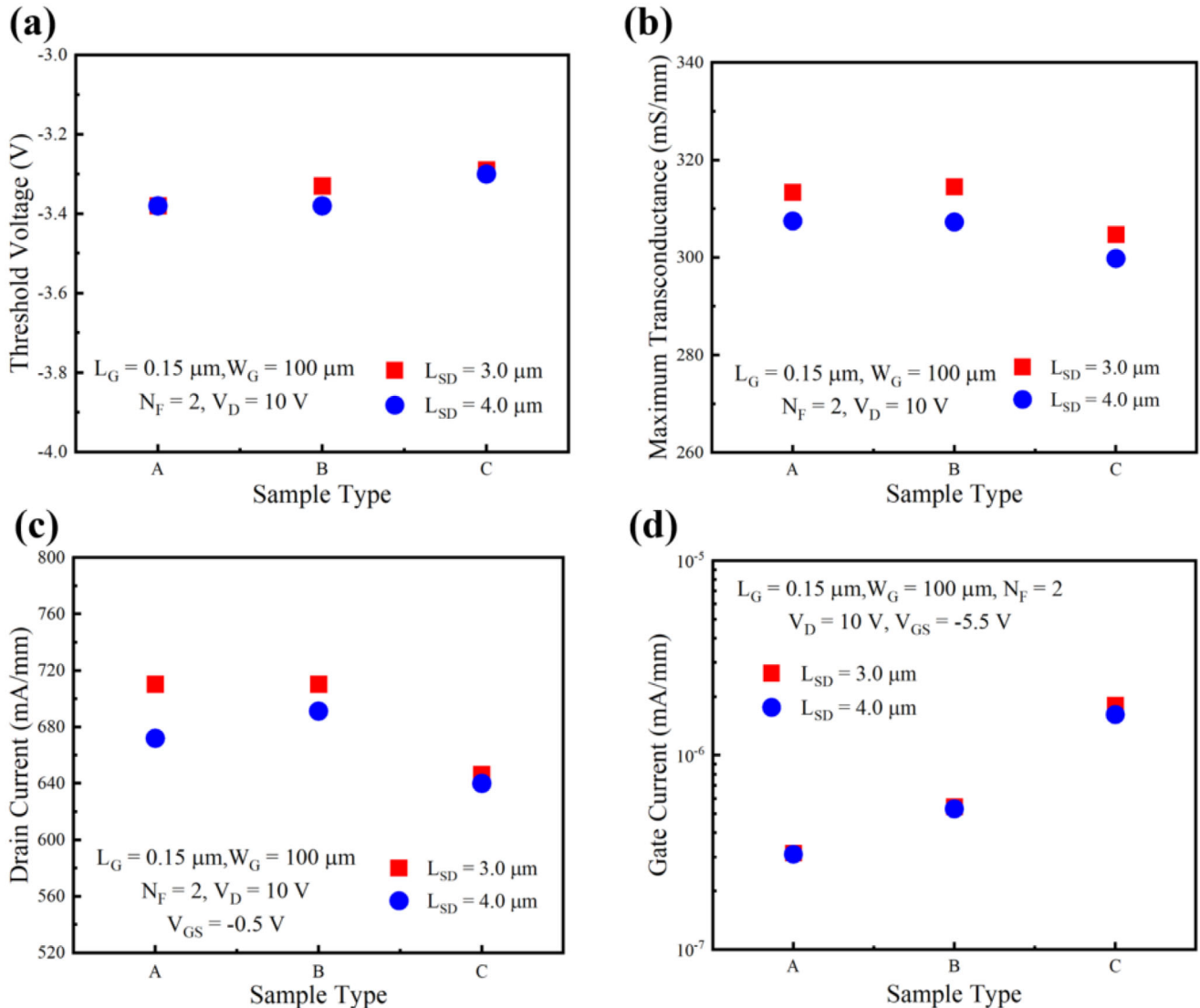


Figure 6. Extracted device parameter comparison corresponding to the passivation layers. a) Threshold voltage, b) maximum transconductance, c) drain current (at $V_{GS} = -0.5 \text{ V}$), and d) drain leakage current (at $V_{GS} = -5.5 \text{ V}$) for various passivation layers.

We have measured the DC characteristics in GaN-based HEMTs for the various passivation layers. As shown in Figure 5a, the fabricated GaN-based HEMTs exhibited excellent pinch-off characteristics at low gate bias ($V_{GS} < -4.0 \text{ V}$). With increasing gate bias, the drain current (I_D) increased and exceeded 750 mA/mm at $V_{GS} = -0.5 \text{ V}$. In Figure 5b, the I_D curves were overlapped in the subthreshold regime. The leakage current was lower at $V_{GS} \leq -4.5 \text{ V}$ in Sample A and Sample B, which was compared with in Sample C. In other words, we have reduced the leakage current by employing the h-BN passivation layer. The typical bell-shaped transconductance (g_m) behavior was observed (Figure 5c). The output characteristics were investigated in Figure 5d. In Sample B and Sample C, the I_D was saturated at $V_{GS} \approx 2.5 \text{ V}$ due to the self-heating effects.^[35–37] However, in Sample A, the I_D was slightly but consistently increased in a range of $2.5 \text{ V} \leq V_{GS} \leq 10.0 \text{ V}$ since, the self-heating effects were diminished by removing the 90 nm-thick SiN pro-

tection. We have measured the breakdown voltage (V_B), which was determined as V_D at $V_{GS} = -6 \text{ V}$ and $I_D = 1 \text{ mA mm}^{-1}$ as shown in Figure 5e. V_B were extracted as 117, 113, and 89 V for Sample A, Sample B, and Sample C with $L_{SD} = 3 \mu\text{m}$, respectively. When the h-BN passivation layer was employed the V_B was increased.

Note that the contact resistances extracted from the TLM method were 0.334, 0.327, and 0.337 $\Omega \text{ mm}$ for Sample A, Sample B, and Sample C, respectively. The passivation system did not affect to the contact resistance of the processed GaN-based HEMTs. Also, the contact resistance difference corresponding to the passivation layer was negligible.

For the precise comparison of the device properties with respect to the passivation system, various device parameters in terms of the threshold voltage (V_{TH}), maximum transconductance ($g_{m,max}$), I_D (at $V_{GS} = -0.5 \text{ V}$), and drain leakage current ($I_{D,leak}$) at ($V_{GS} = -5.5 \text{ V}$) were extracted in Figure 6. V_{TH} was

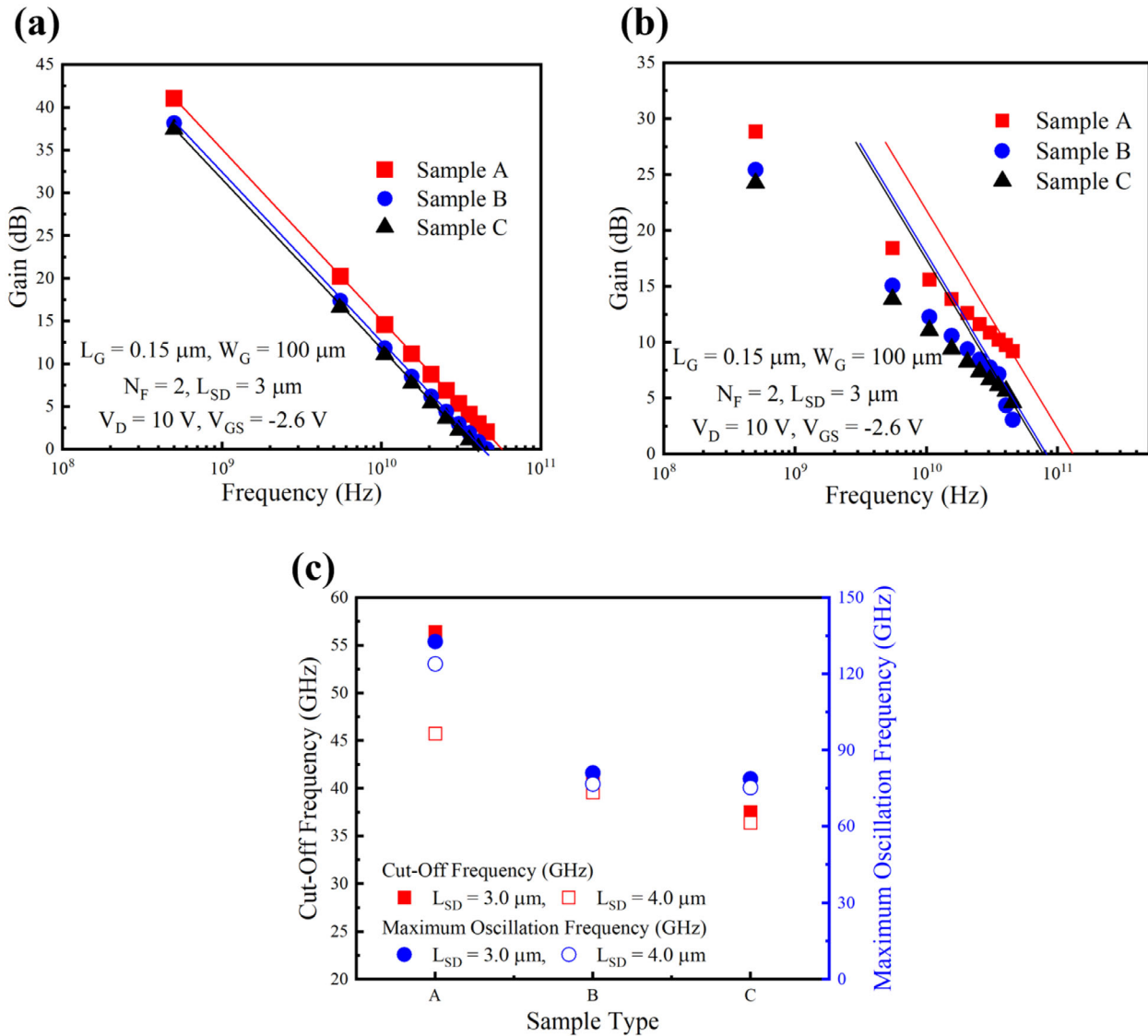


Figure 7. RF performance investigation in GaN-based HEMTs with respect to the various passivation layers. Gain vs frequency for a) current gain cut-off frequency and b) maximum oscillation frequency. c) Extracted the current gain cut-off frequency and maximum oscillation frequency in GaN-based HEMTs for the three different passivation layers.

extracted by plotting $\sqrt{I_D}$ versus V_{GS} and extrapolating the curve to zero drain current.^[38] The $g_{m,max}$ and I_D were slightly lower in Sample C than in Sample A and Sample B. However, the difference was small, which was negligible. The device properties in terms of $g_{m,max}$ and I_D at $V_{GS} = -0.5 \text{ V}$, were enlarged in GaN-based HEMTs for $L_{SD} = 3.0 \mu\text{m}$ compared to the device for $L_{SD} = 4.0 \mu\text{m}$. When the L_{SD} was shrunk, the overall device resistance was reduced and the DC properties were improved. Unlike the other device parameters, the $I_{D,leak}$ was lower when the h-BN was applied as the passivation layer, reflecting that the superior AlGaN/h-BN interface.

In **Figure 7**, the RF characteristics were measured and compared in GaN-based HEMTs for various passivation layers. To extract the f_T and f_{max} , the S-parameters were measured by the network analyzer. The measured S-parameters were converted to the H-parameters for the f_T extraction. We have fitted a linear line

with a -20 dB slope on the H_{21} curve. The extrapolated point of the linear line to the 0 dB was defined as the f_T . For the f_{max} extraction, the measured S-parameters were converted to the maximum stable gain (MSG)/maximum available gain (MAG). Like for the f_T extraction, a linear line with -20 dB slope was fitted at the stability factor $K = 1$. The f_{max} was determined by a point, which was the extrapolated point of the linear line to the 0 dB .

When the L_{SD} was reduced, the g_m was enlarged as shown in **Figures 5c** and **6b**. Indeed, the parasitic capacitances such as C_{gs} and C_{gd} were reduced, which will be shown in **Figure 8a,b**. For these reasons, GaN-based HEMTs for $L_{SD} = 3.0 \mu\text{m}$ exhibited higher f_T and f_{max} when we compared in GaN-based HEMTs for $L_{SD} = 4.0 \mu\text{m}$.

When we compared the Sample B and Sample C, the RF performance was slightly improved in Sample B. The f_T and f_{max} were improved by 9.4% and 2.9%, respectively. By contrast, we

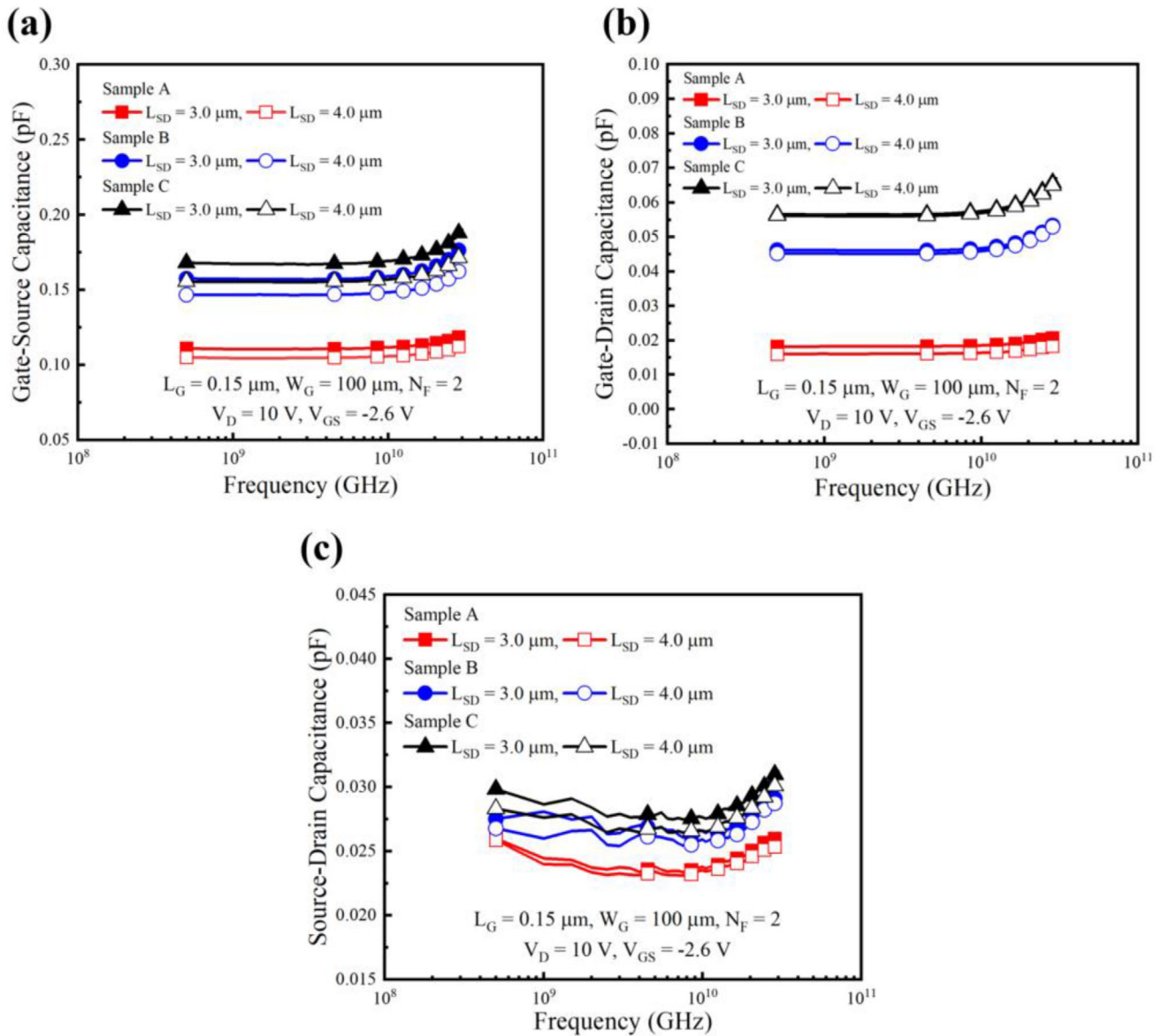


Figure 8. Extraction of the parasitic capacitances linked to the passivation layer and gate structure in GaN-based HEMTs for various passivation layers. a) Gate-source capacitance, b) gate-drain capacitance, and c) source-drain capacitance as a function of frequency.

have achieved a huge RF performance improvement in Sample A. Compared to the Sample C, the f_T and f_{max} were improved by 50.3% and 68.5%, respectively in Sample A.

As shown in Figure 8, we have extracted the parasitic capacitances which were affected by the passivation layer and gate structure to figure out the reason of the RF performance improvement in Sample A. The device capacitances were extracted using equation (1)–(6) from the ref. [19] The S -parameters of the device were measured under Cold FET conditions and subsequently converted into Y -parameters for the capacitance extraction. The parasitic capacitances arising from the external structure and interconnections were identical for the three devices, since their layouts are the same. Therefore, the differences in capacitances shown in Figure 8 represented the variations in the intrinsic ca-

pacitance in terms of C_{gd} , C_{gs} , and C_{ds} , which were caused by differences in the passivation structures.

In Sample B, the parasitic capacitances were slightly reduced compared in Sample C since, the dielectric constant of the h-BN was smaller than that of the SiN. In Sample A, the SiN layer was substituted for an air spacer. And, the dielectric constant of the air spacer was much smaller than that of SiN. As a result, the huge RF improvement was achieved in Sample A.

We have summarized the DC and RF performance achieved from Sample A in this work and compared with other work in Table 1. Note that the other works compared with Sample A featured a gate length of $\approx 0.15 \mu\text{m}$ and utilized a GaN-based HEMTs fabrication process comparable to those used in our study.

Table 1. Summarized DC and RF Performance in Sample A and performance comparison with the competitive researches.

	Sample A [in this work]	Ref. [39]	Ref. [40]	Ref. [41]	Ref. [42]
Maximum transconductance (mS/mm)	315	410	450	470	403
Saturation drain current (A)	715	950	-	1200	999
Breakdown voltage (V)	117	>100	120	84	-
Current gain cut-off frequency (GHz)	56	36	45	40	36
Maximum oscillation frequency (GHz)	134	115	80	-	158

4. Conclusion

This study has demonstrated the feasibility of utilizing the h-BN as a passivation layer in GaN-based HEMTs. An extremely thin h-BN passivation layer and air spacer were successfully employed for the GaN-based HEMTs fabrication. The h-BN passivation layer was grown by MOCVD before the device fabrication due to its very high growth temperature. For the device processing, the SiN protection layer covered the thin h-BN passivation layer. After the T-gate electrode formation, the SiN protection layer was removed by dipping the processed device into the BOE, naturally formed the air spacer under the head of the T-gate electrode. The DC characteristics of the h-BN passivated GaN-based HEMTs were almost identical to the conventional SiN passivated GaN-based HEMTs. On the other hand, the huge improved RF performance in terms of the f_T and f_{max} was obtained in GaN-based HEMTs for the thin h-BN passivation layer and air spacer since, the parasitic capacitances were reduced by the small dielectric constant of the air. As a result, the reduction of the parasitic capacitances, which were related to the passivation layer and T-gate structure was efficient for the improvement of the RF performance in GaN-based HEMTs. However, the device processing should be further optimized to achieve a larger device process margin since, the h-BN was too thin and weak for the conventional GaN-based HEMTs processing.

Acknowledgements

This research was supported by the Civil-Military Technology Cooperation Program (No. 19-CM-BD-05).

Conflict of Interest

The authors declare no conflict of interest.

Data Availability Statement

The data that support the findings of this study are available from the corresponding author upon reasonable request.

Keywords

air spacer, GaN, h-BN, HEMT, passivation

Received: September 14, 2025

Revised: October 20, 2025

Published online:

- [1] Y. Tang, K. Shinohara, D. Regan, A. Corrión, D. Brown, J. Wong, A. Schmitz, H. Fung, S. Kim, M. Micovic, *IEEE Electron. Device Lett.* **2015**, *36*, 549.
- [2] T. Palacios, A. Chakraborty, S. Rajan, C. Poblenz, S. Keller, S. P. DenBaars, J. S. Speck, U. K. Mishra, *IEEE Electron. Device Lett.* **2005**, *26*, 781.
- [3] K. Shinohara, D. C. Regan, Y. Tang, A. L. Corrión, D. F. Brown, J. C. Wong, J. F. Robinson, H. H. Fung, A. Schmitz, T. C. Oh, S. J. Kim, P. S. Chen, R. G. Nagele, A. D. Margomenos, M. Micovic, *IEEE Trans. Electron. Devices* **2013**, *60*, 2982.
- [4] R. Vetry, N. Q. Zhang, S. Keller, U. K. Mishra, *IEEE Trans. Electron Devices* **2001**, *48*, 560.
- [5] B. Green, K. Chu, E. Chumbes, J. Smart, J. Shealy, L. Eastman, *IEEE Electron Device Lett.* **2000**, *21*, 268.
- [6] L. F. Eastman, V. Tilak, J. Smart, B. M. Green, E. M. Chumbes, R. Dimitrov, H. Kim, O. S. Ambacher, N. Weimann, T. Prunty, M. Murphy, W. J. Schaff, J. R. Shealy, *IEEE Trans. Electron Devices* **2001**, *48*, 479.
- [7] T. Hashizume, J. Kotani, H. Hasegawa, *Appl. Phys. Lett.* **2004**, *84*, 4884.
- [8] Z. H. Liu, G. I. Ng, S. Arulkumaran, Y. K. T. Maung, K. L. Teo, S. C. Foo, V. Sahnuganathan, *Appl. Phys. Lett.* **2009**, *95*, 223501.
- [9] P. D. Ye, B. Yang, K. K. Ng, J. Bude, *Appl. Phys. Lett.* **2005**, *86*, 063501.
- [10] S. Arulkumaran, T. Egawa, H. Ishikawa, T. Jimbo, Y. Sano, *Appl. Phys. Lett.* **2004**, *84*, 613.
- [11] S. Arulkumaran, T. Egawa, H. Ishikawa, T. Jimbo, M. Umeno, *Appl. Phys. Lett.* **1998**, *73*, 809.
- [12] W. Lu, V. Kumar, R. Schwindt, E. Piner, I. Adesida, *Solid-State Elec.* **2002**, *46*, 1441.
- [13] A. V. Vertiatikh, L. F. Eastman, W. J. Schaff, T. Prunty, *Electronics Lett.* **2002**, *38*, 388.
- [14] R. Mehandru, B. Luo, J. Kim, F. Ren, B. P. Gila, A. H. Onstine, C. R. Abernathy, S. J. Pearton, D. Gotthold, R. Birkhahn, B. Peres, R. Fitch, J. Gillespie, T. Jenkins, J. Sewell, D. Via, A. Crespo, *Appl. Phys. Lett.* **2003**, *82*, 2530.
- [15] X. Z. Dang, E. T. Yu, E. J. Piner, B. T. McDermott, *J. Appl. Phys.* **2001**, *90*, 1357.
- [16] S.-J. Chang, H.-W. Jung, J.-W. Do, K. J. Cho, J.-J. Kim, Y. J. Jang, H. S. Yoon, H.-K. Ahn, B.-G. Min, H. Kim, J.-M. Yang, H.-S. Kwon, J.-W. Lim, *ECSJ. Solid State Sci. Technol.* **2018**, *7*, N86.
- [17] R. K. Yadav, P. Pathak, R. M. Mehra, *Int. J. Electr. Comput. Eng.* **2017**, *7*, 1839.
- [18] T. Palacios, Y. Dora, A. Chakraborty, C. Sanabria, S. Keller, S. P. DenBaars, U. K. Mishra, *Phys. Status Sol.* **2006**, *203*, 1845.
- [19] A. Jarndal, G. Kompa, *IEEE Trans. Microw. Theory Tech.* **2005**, *53*, 3440.
- [20] K. W. Kobayashi, V. Kumar, *IEEE Microw. Wirel. Compon. Lett.* **2021**, *31*, 885.
- [21] J. R. Kumar, D. Nirmal, J. Ajayan, S. Tayal, *Silicon* **2022**, *14*, 11315.
- [22] D. Dominijanni, E. Giovine, A. Notargiacomo, A. Pantellini, P. Romanini, M. Peroni, A. Nanni, *Microelectron. Eng.* **2011**, *88*, 1927.
- [23] M. Meryleen, T. De, A. K. Panda, *Int. J. Nanoparticles* **2019**, *11*, 113.
- [24] B. H. Lee, R. H. Kim, B. O. Lim, G. W. Choi, H. J. Kim, I. P. Hong, J. H. Lee, *Electron. Lett.* **2013**, *49*, 1013.
- [25] K.-Y. Cheng, S.-C. Wu, C.-J. Yu, T.-W. Wang, J.-H. Liao, M.-C. Wu, *Solid-State Electron.* **2020**, *170*, 107824.
- [26] L. Li, K. Nomato, M. Pan, W. Li, A. Hickman, J. Miller, K. Lee, Z. Hu, S. J. Bader, S. M. Lee, J. C. M. Hwang, D. Jena, H. G. Xing, *IEEE Electron. Device Lett.* **2020**, *41*, 689.

- [27] H. Çakmak, M. Öztürk, E. Özbay, B. Imer, *IEEE Trans. Electron. Devices* **2021**, *68*, 1006.
- [28] P. Murugapandiyar, S. Ravimaran, J. William, K. M. Sundaram, *Superlattices Microstruct.* **2017**, *111*, 1050.
- [29] R. Angamuthu, B. C. Sengodan, M. Anandan, A. Varghese, B. S. Vakkalakula, *Int. J. RF Microw. Comput.-Aided Eng.* **2022**, *32*.
- [30] C.-W. Tsou, C.-Y. Lin, Y.-W. Lian, S. S. Hsu, *IEEE Trans. Electron. Devices* **2015**, *62*, 2675.
- [31] J.-S. Moon, B. Grabar, J. Wong, D. Chuong, E. Arkun, D. V. Morales, P. Chen, C. Malek, D. Fanning, N. Venkatesan, P. Fay, *IEEE Electron. Device Lett.* **2021**, *42*, 796.
- [32] J. S. Moon, R. Grabar, J. Wong, M. Antcliffe, P. Chen, E. Arkun, I. Khalaf, A. Corron, J. Chappell, N. Venkatesan, P. Fay, *Electron. Lett.* **2020**, *56*, 678.
- [33] S. Moon, S.-J. Chang, Y. Kim, O. F. N. Okello, J. Kim, J. Kim, H.-W. Jung, H.-K. Ahn, D.-S. Kim, S.-Y. Choi, J. D. Lee, J.-W. Lim, J. K. Kim, *ACS Appl. Mater. Interfaces* **2021**, *13*, 59440.
- [34] S. Moon, O. F. N. Okello, A. Rousseau, C.-W. Choi, T. Kim, Y. Park, J. Kim, M. Kim, P. Valvin, J. Cho, K. Watanabe, T. Taniguchi, H. Y. Jeong, G. Fugallo, W. Desrat, F. Ding, J. D. Lee, B. Gil, G. Cassabois, S.-Y. Choi, J. K. Kim, *Nat. Mater.* **2025**, 843.
- [35] S. Karmalkar, U. K. Mishra, *IEEE Trans. Electron. Devices* **2001**, *48*, 1515.
- [36] J. Kuzmik, R. Javorka, A. Alam, M. Marso, M. Heuken, P. Cordos, *IEEE Trans. Electron Devices* **2002**, *49*, 1496.
- [37] S.-J. Chang, K.-J. Cho, S.-Y. Lee, H.-H. Jeong, J.-H. Lee, H.-W. Jung, S.-B. Bae, I.-G. Choi, H. Kim, H.-K. Ahn, J.-W. Lim, *Crystals* **2021**, *11*, 1414.
- [38] H. G. Lee, S. Y. Oh, G. Fuller, *IEEE Trans. Electron Dev.* **1982**, *29*, 346.
- [39] Y. Ando, H. Takahashi, R. Makisako, A. Wakejima, J. Sada, *Electronics Lett.* **2023**, *59*, 1.
- [40] L. Zhang, B. Lv, X. Ding, F. Yu, Z. Wang, J. Mo, *ECSJ. Solid State and Tech.* **2024**, *13*, 075001.
- [41] K. M. Bothe, B. Schmukler, S. Ganguly, T. Alcorn, J. Gao, C. Hardiman, E. Jones, D. Namishia, F. Radulescu, J. Barner, J. Fisher, D. A. Gajewski, S. T. Sheppard, J. W. Milligan, presented at *Optically-Defined 150-nm, 28-V GaN HEMT Process for Ka-band*, *Int. Conf. Compound Semiconductor Manufacturing Technology, (CSMANTECH)* 209, Minneapolis, US, April, **2019**.
- [42] M.-W. Lee, C.-W. Chuang, F. Gamiz, E.-Y. Chang, Y.-C. Lin, *Micromachines* **2024**, *15*, 81.